

In Operando Probing of Lithium-Ion Storage on Single-Layer Graphene

Kun Ni, Xiangyang Wang, Zhuchen Tao, Jing Yang, Na Shu, Jianglin Ye, Fei Pan, Jian Xie, Ziqi Tan, Xuemei Sun, Jie Liu, Zhikai Qi, Yanxia Chen, Xiaojun Wu, and Yanwu Zhu*

Despite high-surface area carbons, e.g., graphene-based materials, being investigated as anodes for lithium (Li)-ion batteries, the fundamental mechanism of Li-ion storage on such carbons is insufficiently understood. In this work, the evolution of the electrode/electrolyte interface is probed on a single-layer graphene (SLG) film by performing Raman spectroscopy and Fourier transform infrared spectroscopy when the SLG film is electrochemically cycled as the anode in a half cell. The utilization of SLG eliminates the inevitable intercalation of Li ions in graphite or few-layer graphene, which may have complicated the discussion in previous work. Combining the in situ studies with ex situ observations and ab initio simulations, the formation of solid electrolyte interphase and the structural evolution of SLG are discussed when the SLG is biased in an electrolyte. This study provides new insights into the understanding of Li-ion storage on SLG and suggests how high-surface-area carbons could play proper roles in anodes for Li-ion batteries.


One major challenge in the research of lithium (Li)-ion batteries (LIBs) is to develop electrodes with higher energy and power performances. The way to improve the performance of electrodes includes searching for novel active materials and developing the understanding of Li-storage mechanisms. Among various anode materials considered for LIBs, graphite has been widely utilized via the reversible intercalation of Li ions between graphitic layers in charging and discharging.^[1,2] It is well accepted that the intercalation of Li ions in graphite follows

a staging mechanism and the highest theoretical capacity ($\approx 372 \text{ mAh g}^{-1}$) corresponds to the final intercalation stage (LiC_6).^[2] During the initial cycling, a solid electrolyte interphase (SEI) is formed on the graphite anode due to the deposition of inorganic and organic species which originate from the decomposition or reaction of electrolyte solutions during negative polarization.^[1] The highly reversible intercalation of Li ions and the stable SEI are considered as key factors for the commercial applications of graphite anode in LIBs over the last few decades.^[3–5] In practical applications, one has realized the necessity of controlling the specific surface area (SSA) of graphite to prevent the low initial Coulombic efficiency,^[6,7] but the intrinsic reason remains to be understood.^[1]

To further improve the anode performance of LIBs, nanostructured carbon materials have been widely investigated as supporting scaffolds or active components.^[6,8] Ultrahigh Li-ion storage capacity values (e.g., initial capacities of $\approx 7500 \text{ mAh g}^{-1}$ for graphene nanoflakes,^[9] or $\approx 2811 \text{ mAh g}^{-1}$ for a hierarchical carbon^[10]) have been reported from the anodes made of nanostructured carbons. Such carbons could maintain the high capacity (more than 1000 mAh g^{-1} ,^[6] depending on cycling currents) for hundreds of cycles, but usually demonstrated an initial Coulombic efficiency of lower than 60% (Table S1, Supporting Information). Since nanostructured carbons often possess high SSAs, mechanisms other than intercalation reaction^[2] have been proposed to explain the capacities measured, which are much higher than that of graphite.^[6,8] For example, the presence of Li_2 molecules has been proposed based on a nuclear magnetic resonance analysis of a disordered carbon, leading to a stoichiometry of LiC_2 .^[11] Instead of simple interaction, it seems that the Li–Li interaction on carbon could compete among covalency, ionicity, and metallicity depending on the degree of electron delocalization.^[2] LiC configuration was also suggested by assuming that both carbon atoms in the primitive cell of graphene could adsorb Li ions alternately on both sides.^[12] However, conflicting results from simulations indicated that the Li-ion storage capacity of graphene might be significantly lower than that of graphite,^[13] due to the strong Coulombic repulsion of Li atoms on the opposite sides of the graphene.^[14] Furthermore, Li could be adsorbed on the surface of carbon electrodes,^[2,15] e.g., through the reaction with

K. Ni, X. Wang, Z. Tao, N. Shu, J. Ye, F. Pan, J. Xie, Z. Tan, X. Sun, J. Liu, Z. Qi, Prof. X. Wu, Prof. Y. Zhu
Hefei National Research Center for Physical Sciences at the Microscale
CAS Key Laboratory of Materials for Energy Conversion
Department of Materials Science and Engineering
i-ChEM (Collaborative Innovation Center of Chemistry for Energy Materials)
University of Science and Technology of China
96 Jin Zhai Rd., Hefei, Anhui 230026, P. R. China
E-mail: zhuyanwu@ustc.edu.cn

J. Yang, Prof. Y. Chen
Hefei National Laboratory for Physical Sciences at Microscale
Department of Chemical Physics
University of Science and Technology of China
96 Jin Zhai Rd., Hefei, Anhui 230026, P. R. China

 The ORCID identification number(s) for the author(s) of this article can be found under <https://doi.org/10.1002/adma.201808091>.

DOI: 10.1002/adma.201808091

the grain boundary in polycrystalline carbons^[16] or with the liquid electrolyte on the interface.^[1] Probably related to the situations on carbon, the additional capacity measured from RuO₂ electrode was contributed from the generation of LiOH and the subsequent reversible reaction of LiOH with Li (forming Li₂O and LiH).^[17] Although the proceedings listed above, however, more detailed Li-ion storage on nanostructured carbons is insufficiently understood.^[2]

The challenges in understanding the Li-ion storage in nanostructured carbons partially originate from the complex porosity in most materials reported, and the insufficient techniques for probing the SEI which is related to the former. In such a sense, an operando spectroscopy during the electrochemical measurement may provide valuable information about lithiation/delithiation on carbons. For instance, an in situ Raman study on graphite has verified the phase transition from dilute stage 1 (LiC₇₂) to stage 1 (LiC₆) via three charging plateaus.^[18] The splitting of G peak and shift of 2D peak in the Raman spectra of graphite have been associated with the staging formation of graphite intercalation compound during the initial lithiation.^[3] An in situ Raman study on reduced graphene oxide (rGO) suggested the Li storage on rGO via a surface adsorption mechanism.^[19] An in situ differential electrochemical mass spectroscopy study indicated that the SEI formation on graphite anode includes distinct processes such as the reduction of electrolyte solvent and the formation of lithium alkyl carbonates.^[20] Furthermore, an in situ Fourier transform infrared (FTIR) spectroscopy study on a glassy carbon has detected the solvation/desolvation of Li ions during the electrochemical reaction.^[4] In situ FTIR differential spectroscopy indicated the evolution of oxygen-containing groups from a graphene oxide electrode.^[21] Very recently, an in situ transmission electron microscopy (TEM) study proposed the presence of a super dense, closely packed Li structure between layers in double-layered graphene.^[22] Although numerous experiments,^[3,23] the Li storage on single-layer graphene (SLG) shall be distinct and SLG may provide a neat platform for mimicking the behaviors of Li ions on high-specific surface area carbons while less interfered by the defects or doping/groups.

In this work, in operando Raman spectroscopy and FTIR spectroscopy are performed on SLG made from chemical vapor deposition (CVD) during the electrochemical measurement in a custom-designed cell. By combining ex situ observations of SEI on SLG and density functional theory (DFT) simulations, the evolution of SLG structure and SEI development in the electrochemical cycling are detected. It is found that the adsorption of Li ions on the biased SLG tends to induce defects for further adsorption in the sequential cycling; the avalanche deposition and reaction lead to an amorphized SLG covered by the SEI layer. The Li-contained species embedded in SEI, especially the possible presence of metallic Li may significantly contribute to the ultrahigh specific capacity as typically obtained in many nanostructured carbon anodes.

Figure 1 schematically shows the transfer of SLG grown on Cu by CVD,^[24] and the subsequent assembly of a cell for in situ Raman and FTIR measurements. The detailed experimental description can be found in the Supporting Information. In brief, a wet transfer with assistance of polymethyl methacrylate (PMMA) has been used to transfer the SLG to a CaF₂ crystal,^[25] which is an excellent infrared window while transparent to visible light and yet stable in Li-ion electrolytes.^[4] The SLG/CaF₂ was assembled in a custom-designed sealing cell for electrochemical measurements coupled with Raman or FTIR spectroscopy. The optical image of SLG on Cu in Figure S1a in the Supporting Information shows a clean surface with Cu steps and graphene wrinkles but no significant amount of defects.^[25] The optical (Figure S1b, Supporting Information) and scanning electron microscopy (SEM) (Figure S1c, Supporting Information) images of SLG transferred on a SiO₂/Si substrate following the same transfer procedure described above show the uniform single layer coverage rarely with cracks or PMMA residual, while polycrystalline nucleation sites and grain boundaries are observed as reported previously.^[25,26] The TEM image (Figure S1d, Supporting Information) and selected-area electron diffraction (SAED, Figure S1e, Supporting Information) pattern further indicate the feature of SLG.^[27] Raman spectrum of SLG on SiO₂/Si (Figure S1f, Supporting Information) shows representative signals of SLG with G peak ($\approx 1585\text{ cm}^{-1}$) and 2D peak

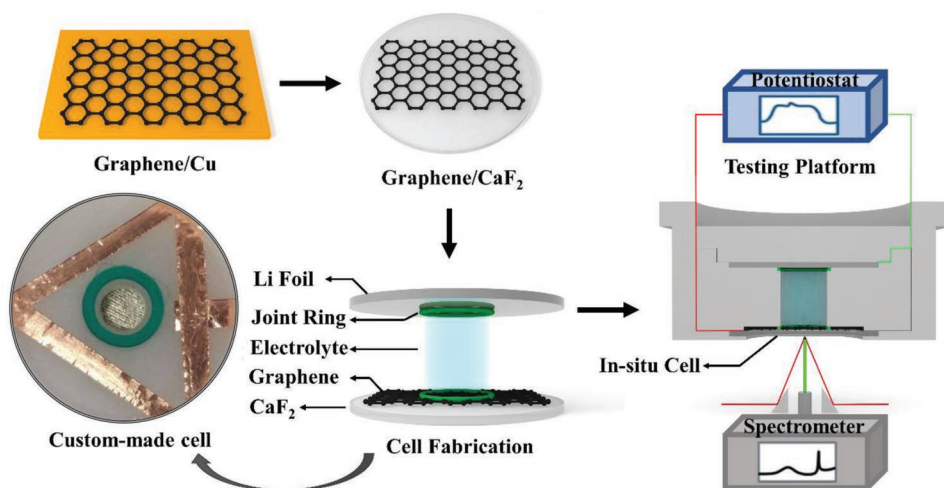


Figure 1. Schematic representation of transfer of SLG grown from Cu foils and in operando system for Raman and FTIR measurements.

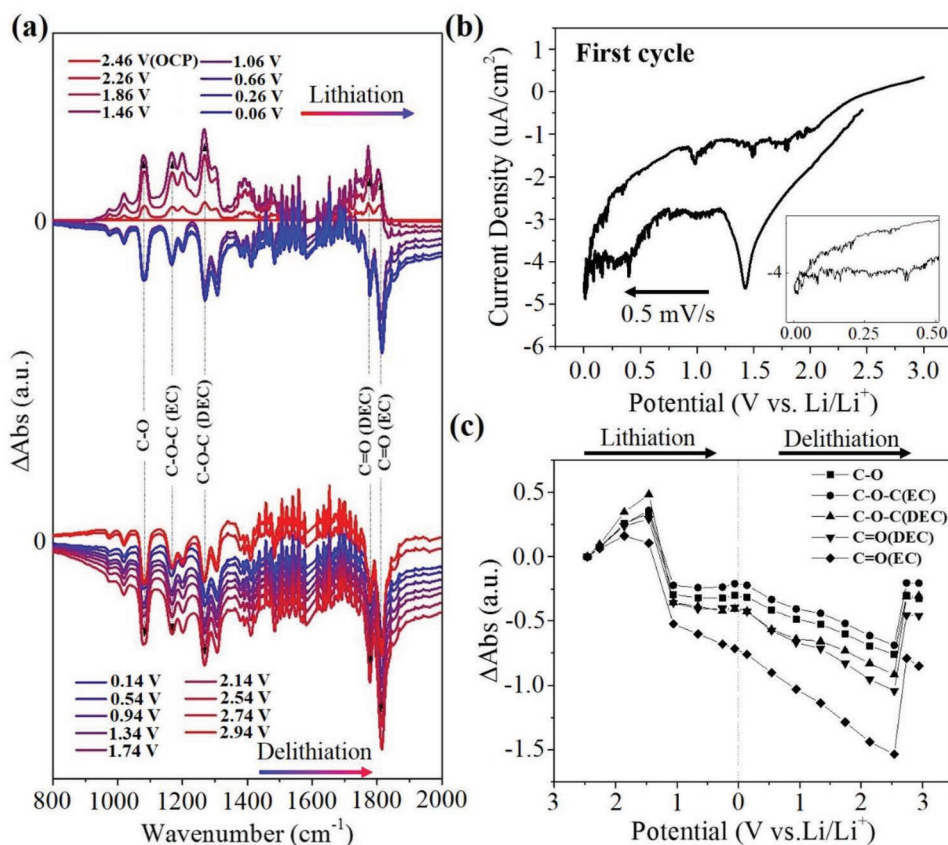


Figure 2. In situ FTIR. a) FTIR spectra on SLG, recorded every 0.4 V in the first electrochemical cycle; b) CV curve measured in 1 M LiPF₆ till 0.001 V potential cut-off. Inset shows the details between 0.001 and 0.50 V; and c) FTIR absorbance depending on potential in lithiation/delithiation.

($\approx 2680\text{ cm}^{-1}$), corresponding to E_{2g} phonons at the Brillouin zone center and the inelastic scattering of two phonons with opposite momentum near the K point, respectively.^[28] The high 2D/G ratio ($I_{2D}/I_G = 2.4$) and negligible D ($\approx 1335\text{ cm}^{-1}$)/D' ($\approx 1615\text{ cm}^{-1}$) peaks suggest that the as-transferred SLG has a low level of defects,^[29,30] as D/D' peaks require defects for activation via an intervalley double-resonance Raman process.^[31]

FTIR reflectivity spectra were obtained using a single beam spectrum measurement as a background, which was performed prior to the electrochemical testing, as shown in Figure S2a in the Supporting Information. By using the attenuated total reflection geometry, the interference from electrolyte has been minimized. The focus was put in the vibration range of $800\text{--}2000\text{ cm}^{-1}$ to highlight chemical bonding at the interface (Figure S2b, Supporting Information), since the broad band in $3200\text{--}3600\text{ cm}^{-1}$ is related to the vibration modes such as from adsorbed water molecules or from the solvents (EC: ethylene carbonate and DEC: diethyl carbonate);^[21] the band in $2700\text{--}3000\text{ cm}^{-1}$ is assigned to bending modes of C–H from the solvents.^[32] **Figure 2a** shows the evolution of FTIR spectra recorded in the first electrochemical cycle, which generates a cyclic voltammetry (CV) curve shown in **Figure 2b**. From the FTIR spectra, main bands attributed to the following vibrations can be identified: C=O ($\approx 1815\text{ cm}^{-1}$, stretching vibration from EC; $\approx 1778\text{ cm}^{-1}$, stretching vibration from DEC), C–O–C ($\approx 1268\text{ cm}^{-1}$, asymmetric stretching vibration from DEC; $\approx 1167\text{ cm}^{-1}$, symmetric

stretching vibration from EC), and C–O ($\approx 1082\text{ cm}^{-1}$, bending vibration),^[32] all of which have been considered closely related to the formation of SEI. Other peaks in the spectra may be assigned to Li₂CO₃ ($1500\text{--}1490\text{ cm}^{-1}$ and $1440\text{--}1430\text{ cm}^{-1}$) and ROCO₂Li ($1650\text{--}1640\text{ cm}^{-1}$ and $\approx 1300\text{ cm}^{-1}$) due to the reaction of electrolyte.^[33] As can be seen from **Figure 2a**, at the beginning of lithiation, the intensity of vibration bands increases first till the maximum at $\approx 1.46\text{ V}$ and then generally decreases in the rest electrochemical process. Correspondingly, a cathodic peak at $\approx 1.43\text{ V}$ is observed in the CV curve in **Figure 2b**, indicating the formation of SEI.^[1] The CV displays a quasi-capacitive behavior with a broad cathodic current minimum between ≈ 0.50 and $\approx 1.00\text{ V}$ when the effect of overpotential is neglected.^[14] For the potentials below $\approx 0.50\text{ V}$ (inset of **Figure 2b**) no remarkable peaks are observed, which is consistent with results from CVD graphene on SiO₂/Si,^[14,34] distinguishing the Li-ion storage on SLG from situations for graphite and FLG. The cathodic current in the CV curve may be partially contributed to the irreversible reduction reaction of electrolyte observed previously,^[14,35] some limited electrochemical kinetics, e.g., caused by the large internal resistance,^[36] and the defects as discussed below. The copper or copper oxide residuals is neglectable since no Raman peaks in selected range or related redox peaks in the CV curve are observed (**Figure S3**, Supporting Information).

Figure 2c summarizes the evolution of FTIR absorbance intensity for the main vibrations mentioned above as a function

of potential. The increased absorption of C–O, C–O–C, and C=O groups at the beginning of cathodic polarization indicates the gathering of solvent molecules and solvated Li ions on the SLG.^[1] This gathering process is similar to the intercalation process occurred in graphite at 0.88V in the cathodic process,^[20] while the single layer nature of SLG may have led to different potentials. The rapid decrease in the absorption for all groups after ≈ 1.46 V suggests that the solvent molecules and solvated Li ions undergo a reduction reaction at the SLG/electrolyte interface,^[37] corresponding to the formation of SEI in the first cycle.^[4] In comparison, EC reduction in the graphite anode occurs at ≈ 0.74 V.^[20] Further decrease in adsorption shall be caused by the slow development of SEI till ≈ 0.06 V. In anodic polarization, e.g., between ≈ 0.14 and ≈ 2.54 V, the desorption of Li ions and the migration of solvated Li-ions to the Li cathode causes the constant decrease in the amount of adsorbed electrolyte

molecules. The subsequent increase from ≈ 2.54 to ≈ 2.74 V may be attributed to the partial oxidation of the solvates at the anodic surface.^[1] It is worth noting that the absorption intensities for all groups after the first cycle are lower than the initial values, implying the irreversible electrochemical reactions in the first cycle. Relatively, the C=O group in EC seems to be more influenced in the formation of SEI. More FTIR measurements in the subsequent cycles show that the SEI continues to develop in the 2nd and 3rd cycles (Figure S4, Supporting Information), while the changes of the groups are much less significant compared to those in the first cycle.

Raman spectra of SLG were collected in the first electrochemical cycle and shown in Figure 3a. D, G, and 2D peaks of SLG in the wet cell remain similar to those of SLG on dry CaF₂ substrate (Figure S5, Supporting Information), while the signals from electrolyte are observed. Upon the lithiation, the

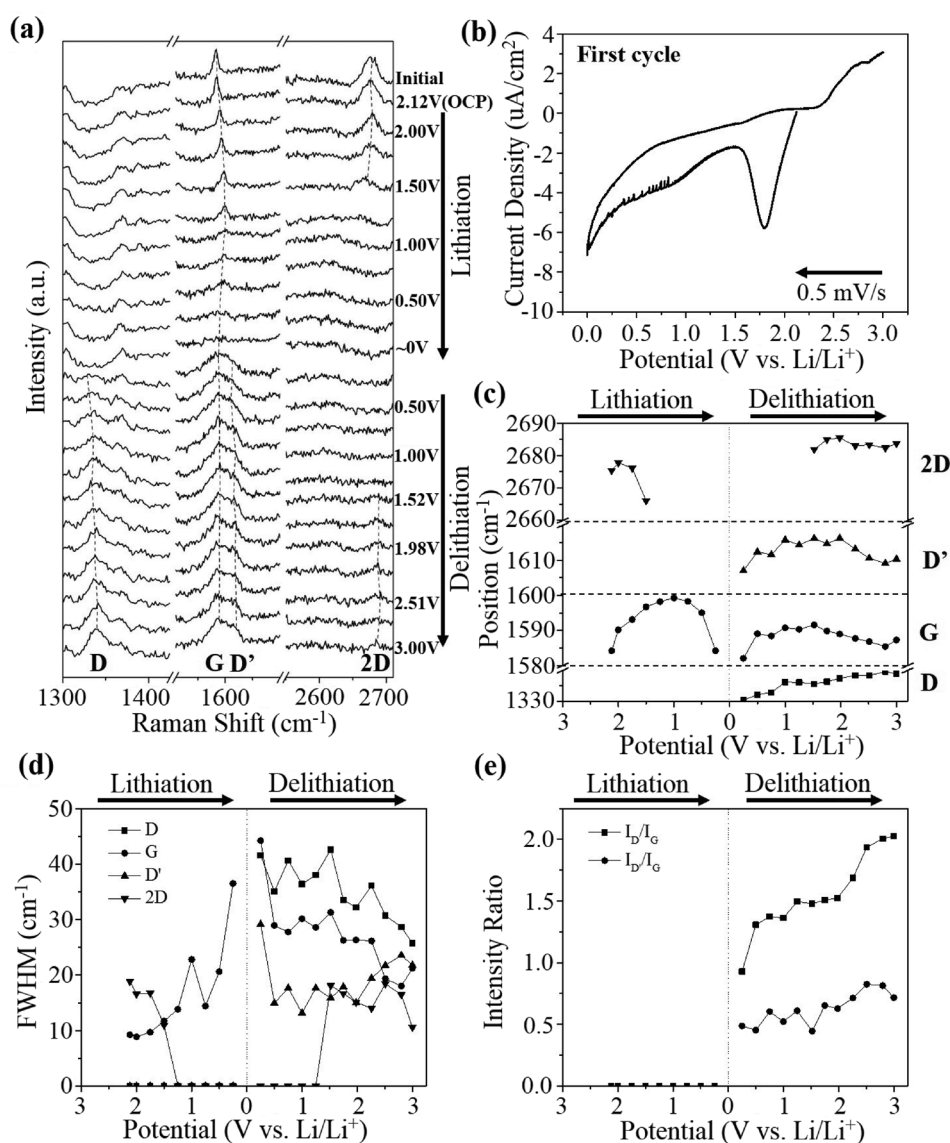


Figure 3. In situ Raman. a) Raman spectra of SLG recorded every 0.25 V in the first electrochemical cycle; b) first-cycle CV curve in 1 M LiPF₆ till 0.001 V potential cut-off; c) peak positions and d) FWHMs of D, G, D', and 2D peaks in lithiation/delithiation; e) I_D/I_G and $I_{D'}/I_G$ ratios as a function of potential.

G peak first shifts to the higher wavenumbers and then back to the lower values, till a nearly complete extinction at ≈ 0.001 V. At the same time, the 2D peak gradually shifts to the lower wavenumbers till an extinction after ≈ 1.50 V. In the first delithiation, D and D' peaks begin to emerge with gradually increasing intensities, while G peak is barely changed. The first CV curve in Figure 3b exhibits a behavior similar to that in Figure 2b except that the peak is located at a little different position (≈ 1.75 V). Obtained from a Lorentzian/Gaussian mix fitting, the change in positions of D, G, D', and 2D peaks is summarized in Figure 3c as a function of potential. The upshift of G peak from ≈ 1584 to ≈ 1599 cm^{-1} upon cathodic polarization shall be attributed to the stiffening of the G-band due to the negative doping.^[14,38] When the polarization potential is reduced to lower than ≈ 1.00 V, the downshift of G peak back to ≈ 1584 cm^{-1} matches well with previous work, suggesting the increased Li doping on SLG.^[14] In the phenomenological staging model of graphite intercalation, Ferrari et al. ever interpreted the similar shift of G peak as the transition of graphite from crystalline to nanocrystalline structure (Stage 1), then to amorphous carbon (Stage 2) and eventually to tetrahedral amorphous carbon (Stage 3).^[39] At the same time, the 2D peak downshifts from ≈ 2675 to ≈ 2666 cm^{-1} and the intensity vanishes at potentials below ≈ 1.50 V, which may be explained by the high background and the influence of SEI, in addition to other factors such as the effect of defects.^[40] In the first delithiation, the G peak shows a blueshift for potentials from ≈ 0.001 to ≈ 1.50 V, then goes downward to ≈ 1587 cm^{-1} at ≈ 3.00 V. The upshift of G peak upon anodic polarization (from ≈ 0.001 to ≈ 1.50 V) is in excellent agreement with the situation in positive doping.^[41] The 2D peak is noticeable above ≈ 1.50 V in the first delithiation, then remains unchanged in terms of position, which may be attributed to the partial reaction of SEI ingredients (affecting 2D peak detection) in the anodic polarization.^[1] Another remarkable feature in delithiation is the appearance of the D and D' peaks, among which the D peak monotonically upshifts to the higher wavenumbers (from 1330 to 1339 cm^{-1}) with increasing intensity (Figure S6a, Supporting Information).^[39]

Figure 3d shows the full width at half maximum (FWHM) of D, G, D', and 2D peaks. G peak has been broadened in lithiation, similar to the situations for biased graphene.^[38,42] Estimated from the relationship between FWHM (G) and average crystallite size (L_a , quantifying line defects) or average distance between nearest defects (L_D , quantifying point defects) proposed by Ribeiro-Soares et al.,^[43] L_a is ≈ 20 nm (>1 μm for the original SLG) and L_D is ≈ 2 nm (∞ for the original SLG) near ≈ 0 V. The remarkable change of D peak has been further identified by the I_D/I_G ratio in Figure 3e, in which the constantly increasing I_D/I_G ratio suggests the continuous development of defects in SLG upon delithiation.^[30] Besides, the nearly linear correlation of A_D/A_G (areal ratio of D to G peak) against FWHM (G) (Figure S7, Supporting Information) also indicates the existence of sp^3 bonding and vacancy defects in graphene.^[44] Although both D and D' modes are defect-induced modes, $I_D/I_{D'}$ was considered to be more sensitive to the topological defects.^[40,45] A $I_D/I_{D'}$ value of 2.07 (Figure S6b, Supporting Information, $A_D/A_{D'}$ of 2.86) has been estimated, relatively close to that from grain boundary defects in graphite ($I_D/I_{D'}$ of ≈ 3.5),^[40] if the influence of electrolyte on Raman is neglected.

In the second electrochemical cycle, nearly periodic appearance and disappearance of D and D' peaks are observed, as shown in Figure S8 in the Supporting Information. The D and D' peaks are barely changed in the third cycle, indicating that the SLG has experienced an irreversible structural change and the defects would maintain after three electrochemical cycles.

To further investigate the surface change on SLG after the electrochemical measurements, ex situ optical photography and Raman spectroscopy/mapping were conducted before and after three electrochemical cycles; the results are shown in Figure S9 in the Supporting Information. As shown in Figure S9a,b in the Supporting Information, the SLG on SiO_2/Si or CaF_2 substrates shows uniform contrast with few cracks, low I_D/I_G and $I_{D'}/I_G$ yet high I_{2D}/I_G ratios, suggesting the robust quality of SLG in transfer.^[27,29] After the SLG is subject to three electrochemical cycles and successive cleaning by DEC and ethanol, the images in Figure S9c in the Supporting Information show the largely enhanced and uniformly distributed I_D/I_G and $I_{D'}/I_G$ ratios in the mapping area. At the same time, the I_{2D}/I_G ratio is significantly reduced, while the mapping distribution is nonuniform. Considering the results from the in situ measurements, it can be concluded that a large amount of disorders and defects have been developed in SLG after the electrochemical cycles. Ex situ SEM and TEM were performed to further investigate the morphological and structural changes on SLG, as shown in Figure 4. From the cross-section SEM image (Figure 4a) of SLG on CaF_2 after three electrochemical cycles, an uneven SEI layer is observed with a thickness from ≈ 120 nm to more than ≈ 500 nm. The typical TEM image of the layer shown in Figure 4b, which was obtained by directly collecting the sample using a TEM Cu grid, reveals the presence of both amorphous and crystallized components in the layer. It seems that the amorphous phase is porous and less dense compared to the crystallized component. By zooming into the dense area, the high resolution transmission electron microscopy (HRTEM) image in Figure 4c shows the presence of nanocrystallites with lattice fringes ascribed to Li_2O (JCPDS#12-0254), Li_2O_2 (JCPDS#09-0355), and LiF (JCPDS#45-1460), respectively. The SAED pattern in Figure 4c shows rings corresponding to Li_2O_2 and Li_2O as well. The HRTEM image in Figure 4d shows the morphology of the component near the SLG, which was taken by collecting samples from the inner layer. From the image a lattice fringe of 2.48 Å is estimated, well consistent to the fast Fourier transformation (FFT, upper inset of Figure 4d) of the area marked by the dashed square. Together with the SAED pattern (bottom inset of Figure 4d), the presence of polycrystalline Li (JCPDS#15-0401) in the inner layer of SEI is considered.^[46] It is worth noting that Li layers were proposed to form on the exposed graphene surface close to edges of FLG.^[47]

The observed structural change in SLG upon electrochemical cycling is attributed to a multitude of complex factors, such as Li adsorption,^[48] topological defect development,^[49] and grain boundary evolution^[50] induced in the electrochemical process. Defects in 2D crystals mainly refer to point defects and line defects.^[51] To simplify the discussion, a Stone–Wales (SW) (5-7-7-5) defect,^[52] generated by reconstruction of a graphene lattice (switching between pentagons, hexagons, and heptagons), is constructed for absorbing Li atoms and the detailed construction is shown in Figure S10 in the Supporting Information. SW

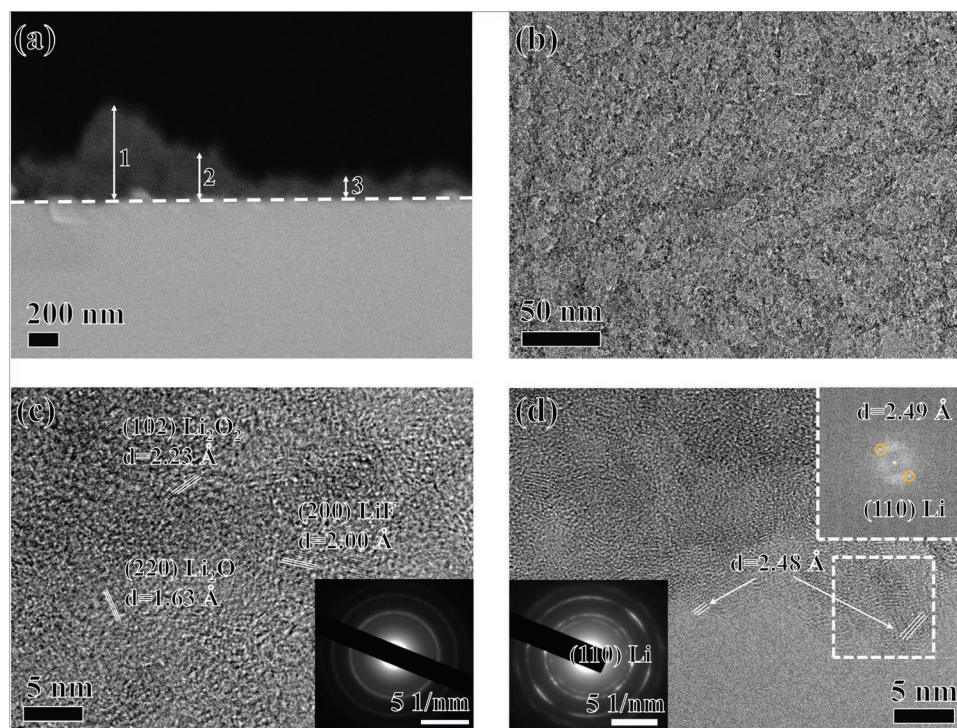


Figure 4. Ex situ SEM and TEM. a) Typical SEM image of SLG anode after three electrochemical cycles. Scale: 1 \approx 568 nm, 2 \approx 275 nm, and 3 \approx 124 nm. b) Typical TEM image of SEI. c) HRTEM image showing lattice fringes in SEI. Inset shows the corresponding SAED pattern. d) HRTEM image showing the lattice fringes possibly attributed to metallic Li. Inset shows SAED pattern (bottom) and FFT image (top) of the marked area.

and single-vacancy (SV) defects were chosen for discussion as they are thought as the basic and representative defects in graphene.^[51] The line defects can be considered as a line of reconstructed point defects with or without dangling bonds.^[53] Specifically, the transition state (TS) barrier, formation energy, and crystal orbital Hamilton populations (COHP) were calculated and analyzed for the adsorption of different numbers of Li atoms on SLG containing a SW (5-7-7-5) defect in a $5 \times 5 \times 1$ supercell. The detailed method can be found in the Supporting Information.

As shown in **Figure 5a**, the calculation indicates that increasing the number of adsorbed Li nearby a C–C bond gradually reduces the TS barrier and formation energy of SW (5-7-7-5) defect. In the $5 \times 5 \times 1$ supercell, the TS barrier energy is reduced from 9.36 to 6.10 eV when three Li atoms are adsorbed on SLG. Correspondingly, the formation energy is gradually reduced from 5.28 to 3.28 eV when the number of Li is increased from 0 to 3 (Figure S11, Supporting Information). Such results suggest that the introduction of Li favors the formation of SW (5-7-7-5) defects both in kinetics and in thermodynamics. To achieve the higher Li capacity, the formation energy of SW (5-7-7-5) defect with more Li atoms was also calculated (Figure S11b, Supporting Information), based on which the formation energy further decreases to 2.35 eV for a stoichiometry of $\text{Li}_{0.9}\text{C}_3$. To estimate the contribution from bonding, nonbonding, and antibonding in the specific pair-pair interaction, COHP has been obtained using a tight-binding approach based on the partitioning of the band energy in terms of orbital-pair contributions.^[54] As shown in Figure 5b, the COHP of C–C interactions in SLG is ≈ 0 at the Fermi energy (0 eV) for the pristine SLG, but shows an obvious antibonding

(positive) peak nearby the Fermi energy when the Li adsorption is introduced. The antibonding peak gradually shifts downward with increasing number of Li, resulting in more antibonding contribution below the Fermi surface and thus the weakening of C–C bonding. This result supports the conclusion that the adsorption of Li favors the formation of defects from the electronic structure aspect.

The deposition of Li on carbon is of debate due to the challenges for distinguishing metallic Li from its oxides; superdense multilayer Li deposition has been recently proposed between layers of bilayer graphene by in situ low-voltage TEM.^[22] In contrast to a low level of Li loading such as single layer adsorption on SLG,^[55] herein Li atoms were added one by one onto the pristine SLG or defective SLG, followed by the optimization of geometry structure (detailed methodology described in the Supporting Information). As shown in Figure 5c,d, an ABC closely packed structure is formed on pristine SLG, while an AB closely packed structure formed on the SLG with SV defect when four-layer Li is considered for both situations (together with two-layer Li and three-layer Li, shown in Figure S12 in the Supporting Information). From the deformation charge density for four-layer Li (Figure 5e,f), we can see that the charge transfer has been enhanced for the SLG with SV defect and the transfer mainly occurs between SLG and the 1st Li layer. The same conclusion is achieved for the two-layer or three-layer Li on pristine SLG or SLG with 1 SV/2 SV/3 SV defects (Figure S13, Supporting Information). On the other hand, when the Li deposition on multilayered graphene stacking is considered (Figure S14, Supporting Information), it is found the charge transfer to the top graphene layer (directly connected to Li) is

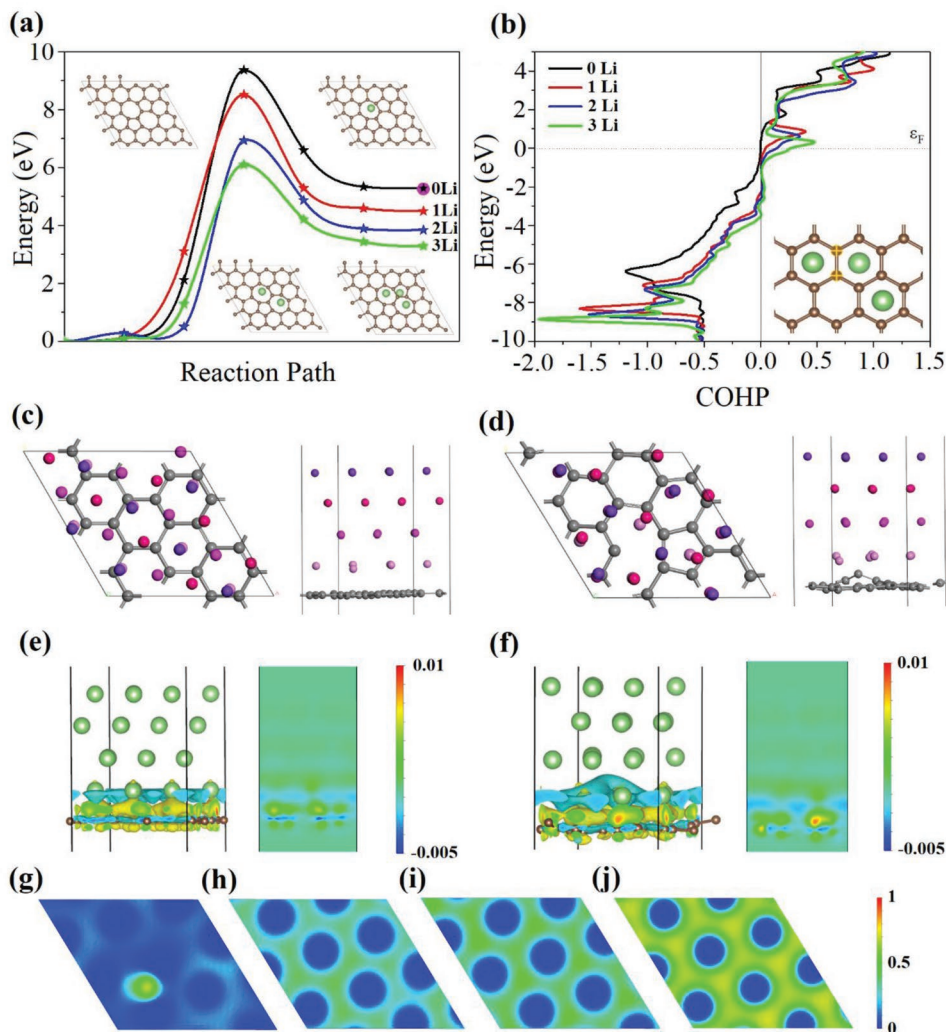


Figure 5. DFT simulations. a) Reaction path and formation energy of Stone–Wales (5-7-7-5) defects for different numbers of adsorbed Li. Inset shows schematic representation of $5 \times 5 \times 1$ supercell configuration of SLG for different adsorbing situations. The purple dot at the end of ‘0 Li’ line corresponds to a formation energy of 5.26 eV.^[51] b) COHP for the specific C–C interactions for different numbers of adsorbed Li. Inset shows the C–C interaction; brown and green balls denote C and Li atoms, respectively. c, d) Top view and side view of four-layer close-packed Li adsorbed on: c) pristine graphene and d) SLG with one SV defect in one simulation cell. e, f) Deformation charge density of four-layer Li adsorbed on: e) pristine SLG and f) SLG with one SV defect in one simulation cell. The iso surface value is $0.0015 \text{ e Bohr}^{-3}$. The 2D mapping on the right side in (e) or (f) corresponds to a slice vertical to the $\langle 100 \rangle$ direction of the simulation cell at the 0.0 fractional coordinate. g–j) 2D distribution of ELF with slice position at the 1st Li layer (g), the 2nd Li layer (h), the 3rd Li layer (i), and the 4th Li layer (j).

reduced with the layer number, indicating that graphite has the higher structural stability than SLG during lithiation. Electron localization function (ELF, details in Supporting Information) analysis was also performed to clarify the electronic property of Li layers on SLG,^[56] and the 2D ELF distribution is shown in Figure 5g–j. As we can see, the 1st layer of Li is highly ionic, corresponding to a charge transfer from Li to graphene, while the 2nd layer of Li is less ionic than the 1st layer. Specifically, the ELF value of the 3rd Li layer is close to 0.5, showing the feature of metallic Li (Figure S15a,b, Supporting Information). The 4th layer shows the localized feature due to the surface state. The similar results are obtained from two-layer and three-layer Li layers on SLG with different concentrations of defects (Figure S15c–p, Supporting Information), leading to a general understanding that Li tends to be metallic for the stacking of

more than three layers. It is worth noting that a similar closely packed structure of Li has also proposed in bilayer graphene.^[22]

Based on the discussion above, a Li-storage mechanism on SLG is schematically summarized in Figure 6. The first lithiation process can be roughly separated into three steps: Step I (OCP to $\approx -1.00 \text{ V}$), gathering and reduction reaction of solvent molecules and solvated Li ions on SLG surface, and beginning formation of SEI; Step II (≈ -1.00 to $\approx -0.50 \text{ V}$), deposition of Li on SLG and development of defects or grain boundaries in SLG; and Step III (≈ -0.50 to $\approx -0.001 \text{ V}$), more deposition of Li and further evolution of SLG structure. It is worth nothing that the electron doping, Li adsorption/deposition, and development of defects in SLG anode may occur simultaneously but with distinct degree for each process in each step. Due to the electron delocalization, part of adsorbed Li ions may be transformed to more metallic

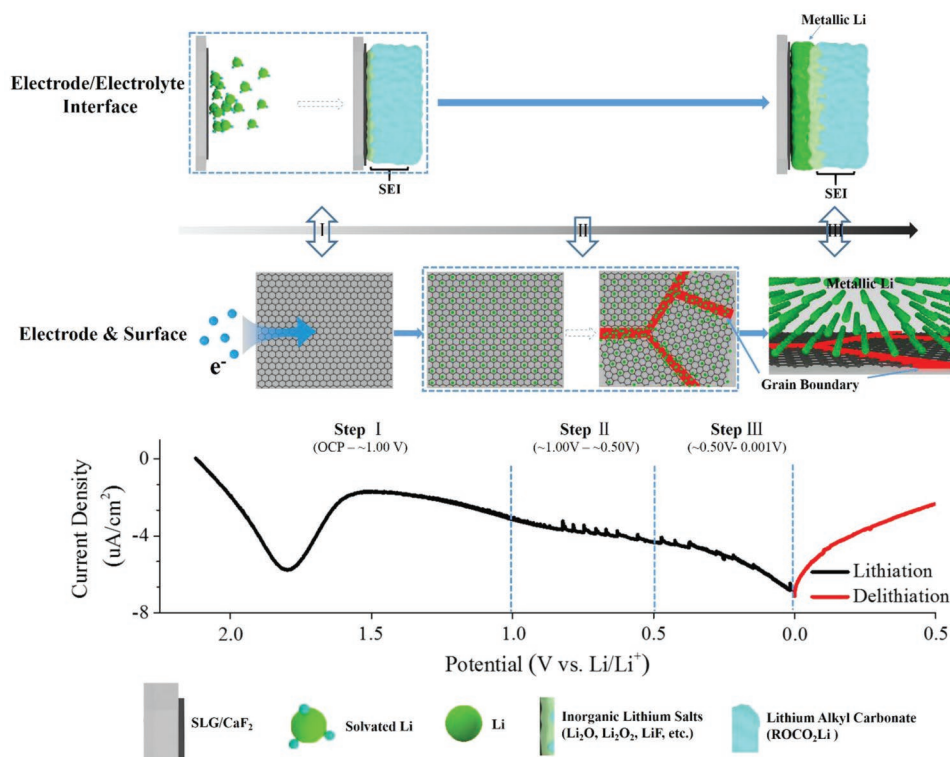


Figure 6. Schematic representation of lithium-storage mechanism in first-cycle lithiation.

Li layers, which could be imbedded inside the SEI layer. In the sequential delithiation, the defects/amorphous phase in SLG is further developed with the partial desorption of Li. The following cycling stabilizes the SEI and the structural change of SLG. It is worth noting that the defects may act as “anchors” in the delithiation, partially contributing to the irreversible CV.

Estimated from the CV measurement (Figure 2b), the total charge stored on SLG in the first lithiation is $\approx 7.60 \text{ mC cm}^{-2}$, which is ≈ 75 times the theoretical capacity of graphite for LiC_6 ($101.82 \text{ } \mu\text{C cm}^{-2}$).^[34] Such a value would lead to an extremely high initial specific capacity of up to $\approx 28\,000 \text{ mAh g}^{-1}$ if the mass of SLG ($7.60 \times 10^{-8} \text{ g cm}^{-2}$) is solely used to normalize the capacity. By integrating the cathodic peak in CV, the charge consumed in the electrolyte reduction/SEI formation is estimated as $\approx 2.84 \text{ mC cm}^{-2}$, resulting in an irreversible capacity loss of $\approx 37.30\%$ in the first electrochemical cycle. The result may explain the low initial Coulombic efficiencies (usually less than 60%) typically observed for nanostructured carbon materials (Table S1, Supporting Information). Even considering the theoretical Li-storage capacity of double-sided SLG (LiC_3 , $\approx 0.20 \text{ mC cm}^{-2}$), the extra Li-storage capacity on SLG still reaches $\approx 4.56 \text{ mC cm}^{-2}$ in the first cycle, corresponding to the theoretical capacity of 6.15 nm thick metallic Li. CV of SLG on CaF_2 was also conducted at different cut-off potentials (Figure S16, Supporting Information), from which the extra capacity in the initial lithiation is estimated as $\approx 1.33 \text{ mC cm}^{-2}$ for 0.10 V cut-off or $\approx 0.23 \text{ mC cm}^{-2}$ for 0.30 V cut-off, respectively, by assuming that the SEI layer consumes the similar amount of charges for different cut-off potentials. Furthermore, the total capacity for $\approx 0 \text{ V}$ cut-off remains ≈ 7.24 and

$\approx 4.96 \text{ mC cm}^{-2}$ in the 2nd and 3rd CV cycle, respectively, close to the reported capacity difference between SLG/Cu and Cu.^[57] After 20 cycles of measurement, the capacity degrades to $\approx 0.75 \text{ mC cm}^{-2}$ (Figure S17, Supporting Information), close to the high end of the values ($\approx 2700 \text{ mAh g}^{-1}$) reported from the nanostructured carbons if the initial capacity is solely normalized to the mass of SLG (Table S1, Supporting Information). Combing all the information, although it is still challenging to confirm the presence of metallic Li under the current conditions,^[22] we tentatively consider that the reversible deposition of Li layers on SLG could be one important contribution to the ultrahigh specific capacity of SLG.

In this work, in operando Raman and FTIR studies have been performed on SLG films grown from CVD upon the lithiation/delithiation. It is found that the gathering and reduction of solvent and solvates in lithiation triggers the formation of SEI which is stabilized in the following cycling. The adsorption/desorption of Li ions on the biased SLG readily induces defects in SLG, which then turns the SLG into a phase full of defects. The simulation verifies the thermodynamically enhanced process of defect formation due to the Li adsorption, the significant charge transfer between Li and SLG with defects, leading to the deposition of closely packed Li layers on the SLG near 0 V versus Li/Li^+ and the metallic property when more than three layers of Li are adsorbed. The ex situ observation has traced the presence of metallic Li in the inner SEI layer. Together with other factors to be discovered, the consumption of Li by SEI/defects and the deposition of Li stacking on SLG could explain the low initial Coulombic efficiency yet the ultrahigh specific capacity typically measured from nanostructured carbon anodes.

Supporting Information

Supporting Information is available from the Wiley Online Library or from the author.

Acknowledgements

K.N. and X.W. contributed equally to this work. This work was supported by Natural Science Foundation of China (51772282) and funding from Hefei Center for Physical Science and Technology.

Conflict of Interest

The authors declare no conflict of interest.

Keywords

density functional theory, graphene, in operando, lithium-ion storage

Received: December 15, 2018

Revised: March 4, 2019

Published online:

- [1] S. J. An, J. Li, C. Daniel, D. Mohanty, S. Nagpure, D. L. W. Iii, *Carbon* **2016**, *105*, 52.
- [2] N. A. Kaskhedikar, J. Maier, *Adv. Mater.* **2009**, *21*, 2664.
- [3] C. Sole, N. E. Drewett, L. J. Hardwick, *Faraday Discuss.* **2014**, *172*, 223.
- [4] S. Pérez-Villar, P. Lanz, H. Schneider, P. Novák, *Electrochim. Acta* **2013**, *106*, 506.
- [5] M. Nie, D. P. Abraham, D. M. Seo, Y. Chen, A. Bose, B. L. Lucht, *J. Phys. Chem. C* **2013**, *117*, 25381.
- [6] L. Shi, Y. Chen, G. Chen, Y. Wang, X. Chen, H. Song, *Carbon* **2017**, *123*, 186.
- [7] X. Y. Yue, W. Sun, J. Zhang, F. Wang, Y. X. Yang, C. Y. Lu, Z. H. Wang, D. Rooney, K. N. Sun, *J. Power Sources* **2016**, *331*, 10.
- [8] Z. Zheng, X. Zhang, F. Pei, Y. Dai, X. Fang, T. Wang, N. Zheng, *J. Mater. Chem. A* **2015**, *3*, 19800.
- [9] Y. Fang, Y. Y. Lv, R. C. Che, H. Y. Wu, X. H. Zhang, D. Gu, G. F. Zheng, D. Y. Zhao, *J. Am. Chem. Soc.* **2013**, *135*, 1524.
- [10] X. Q. Yang, C. Wei, C. C. Sun, X. X. Li, Y. Chen, *J. Alloys Compd.* **2017**, *693*, 777.
- [11] K. Sato, M. Noguchi, A. Demachi, N. Oki, M. Endo, *Science* **1994**, *264*, 556.
- [12] E. Lee, K. A. Persson, *Nano Lett.* **2012**, *12*, 4624.
- [13] C. Ataca, E. Akturk, S. Ciraci, H. Ustunel, *Appl. Phys. Lett.* **2008**, *93*, 043123.
- [14] E. Pollak, B. Geng, K. J. Jeon, I. T. Lucas, T. J. Richardson, F. Wang, R. Kostecki, *Nano Lett.* **2010**, *10*, 3386.
- [15] J. Jamnik, J. Maier, *Phys. Chem. Chem. Phys.* **2003**, *5*, 5215.
- [16] N. Takami, A. Satoh, M. Oguchi, H. Sasaki, T. Ohsaki, *J. Power Sources* **1997**, *68*, 283.
- [17] Y. Y. Hu, Z. Liu, K. W. Nam, O. J. Borkiewicz, J. Cheng, X. Hua, M. T. Dunstan, X. Yu, K. M. Wiaderek, L. S. Du, K. W. Chapman, P. J. Chupas, X. Q. Yang, C. P. Grey, *Nat. Mater.* **2013**, *12*, 1130.
- [18] M. Inaba, H. Yoshida, Z. Ogumi, T. Abe, Y. Mizutani, M. Asano, *J. Electrochem. Soc.* **1995**, *142*, 20.
- [19] W. Tang, B. M. Goh, M. Y. Hu, C. Wan, B. B. Tian, X. C. Deng, C. X. Peng, M. Lin, J. Z. Hu, K. P. Loh, *J. Phys. Chem. C* **2016**, *120*, 2600.
- [20] T. Liu, L. Lin, X. Bi, L. Tian, K. Yang, J. Liu, M. Li, Z. Chen, J. Lu, K. Amine, K. Xu, F. Pan, *Nat. Nanotechnol.* **2019**, *14*, 50.
- [21] A. Viinikanoja, J. Kauppila, P. Damlin, M. Suominen, C. Kvarnstrom, *Phys. Chem. Chem. Phys.* **2015**, *17*, 12115.
- [22] M. Kuhne, F. Borrner, S. Fecher, M. Ghorbani-Asl, J. Biskupek, D. Samuelis, A. V. Krasheninnikov, U. Kaiser, J. H. Smet, *Nature* **2018**, *564*, 234.
- [23] a) J.-B. Wu, M.-L. Lin, X. Cong, H.-N. Liu, P.-H. Tan, *Chem. Soc. Rev.* **2018**, *47*, 1822; b) P. Harks, F. Mulder, P. Notten, *J. Power Sources* **2015**, *288*, 92; c) V. Stancovski, S. Badilescu, *J. Appl. Electrochem.* **2014**, *44*, 23.
- [24] X. Li, W. Cai, J. An, S. Kim, J. Nah, D. Yang, R. Piner, A. Velamakanni, I. Jung, E. Tutuc, S. K. Banerjee, L. Colombo, R. S. Ruoff, *Science* **2009**, *324*, 1312.
- [25] X. Li, Y. Zhu, W. Cai, M. Borysiak, B. Han, D. Chen, R. D. Piner, L. Colombo, R. S. Ruoff, *Nano Lett.* **2009**, *9*, 4359.
- [26] H. Ji, X. Zhao, Z. Qiao, J. Jung, Y. Zhu, Y. Lu, L. L. Zhang, A. H. Macdonald, R. S. Ruoff, *Nat. Commun.* **2014**, *5*, 3317.
- [27] Z. Tu, Z. Liu, Y. Li, F. Yang, L. Zhang, Z. Zhao, C. Xu, S. Wu, H. Liu, H. Yang, *Carbon* **2014**, *73*, 252.
- [28] D. C. Elias, R. R. Nair, T. M. Mohiuddin, S. V. Morozov, P. Blake, M. P. Halsall, A. C. Ferrari, D. W. Boukhvalov, M. I. Katsnelson, A. K. Geim, K. S. Novoselov, *Science* **2009**, *323*, 610.
- [29] A. C. Ferrari, J. C. Meyer, V. Scardaci, C. Casiraghi, M. Lazzeri, F. Mauri, S. Piscanec, D. Jiang, K. S. Novoselov, S. Roth, A. K. Geim, *Phys. Rev. Lett.* **2006**, *97*, 187401.
- [30] L. Jaber-Ansari, K. P. Puntambekar, H. Tavassol, H. Yildirim, A. Kinaci, R. Kumar, S. J. Saldana, A. A. Gewirth, J. P. Greeley, M. K. Y. Chan, M. C. Hersam, *ACS Appl. Mater. Interfaces* **2014**, *6*, 17626.
- [31] M. S. Dresselhaus, A. Jorio, M. Hofmann, G. Dresselhaus, R. Saito, *Nano Lett.* **2010**, *10*, 751.
- [32] M. Moshkovich, M. Cojocar, H. E. Gottlieb, D. Aurbach, *J. Electroanal. Chem.* **2001**, *497*, 84.
- [33] C. R. Yang, Y. Y. Wang, C. C. Wan, *J. Power Sources* **1998**, *72*, 66.
- [34] J. Hui, M. Burgess, J. Zhang, J. Rodriguez-Lopez, *ACS Nano* **2016**, *10*, 4248.
- [35] J. B. Kerr, S. E. Sloop, G. Liu, Y. B. Han, J. Hou, S. Wang, *J. Power Sources* **2002**, *110*, 389.
- [36] M. D. Levi, D. Aurbach, *J. Phys. Chem. B* **1997**, *101*, 4630.
- [37] S. B. Lee, S. I. Pyun, *Carbon* **2002**, *40*, 2333.
- [38] A. Das, S. Pisana, B. Chakraborty, S. Piscanec, S. K. Saha, U. V. Waghmare, K. S. Novoselov, H. R. Krishnamurthy, A. K. Geim, A. C. Ferrari, A. K. Sood, *Nat. Nanotechnol.* **2008**, *3*, 210.
- [39] A. C. Ferrari, J. Robertson, *Phys. Rev. B* **2000**, *61*, 14095.
- [40] A. Eckmann, A. Felten, A. Mishchenko, L. Britnell, R. Krupke, K. S. Novoselov, C. Casiraghi, *Nano Lett.* **2012**, *12*, 3925.
- [41] M. Kalbac, A. Reina-Cecco, H. Farhat, J. Kong, L. Kavan, M. S. Dresselhaus, *ACS Nano* **2010**, *4*, 6055.
- [42] J. H. Zhong, J. Y. Liu, Q. Y. Li, M. G. Li, Z. C. Zeng, S. Hu, D. Y. Wu, W. W. Cai, B. Ren, *Electrochim. Acta* **2013**, *110*, 754.
- [43] J. Ribeiro-Soares, M. E. Oliveros, C. Garin, M. V. David, L. G. P. Martins, C. A. Almeida, E. H. Martins-Ferreira, K. Takai, T. Enoki, R. Magalhaes-Paniago, A. Malachias, A. Jorio, B. S. Archanjo, C. A. Achete, L. G. Cancado, *Carbon* **2015**, *95*, 646.
- [44] A. Eckmann, A. Felten, I. Verzhbitskiy, R. Davey, C. Casiraghi, *Phys. Rev. B* **2013**, *88*, 41.
- [45] M. V. Bracamonte, G. I. Lacconi, S. E. Urreta, L. E. F. F. Torres, *J. Phys. Chem. C* **2014**, *118*, 15455.
- [46] a) X. Wang, M. Zhang, J. Alvarado, S. Wang, M. Sina, B. Lu, J. Bouwer, W. Xu, J. Xiao, J. G. Zhang, J. Liu, Y. S. Meng, *Nano Lett.* **2017**, *17*, 7606; b) H. Ye, S. Xin, Y. X. Yin, J. Y. Li, Y. G. Guo, L. J. Wan, *J. Am. Chem. Soc.* **2017**, *139*, 5916.
- [47] F. J. Sonia, M. K. Jangid, B. Ananthoju, M. Aslam, P. Johari, A. Mukhopadhyay, *J. Mater. Chem. A* **2017**, *5*, 8662.

- [48] X. Fan, W. T. Zheng, J. L. Kuo, *ACS Appl. Mater. Interfaces* **2012**, *4*, 2432.
- [49] H. Yildirim, A. Kinaci, Z. J. Zhao, M. K. Chan, J. P. Greeley, *ACS Appl. Mater. Interfaces* **2014**, *6*, 21141.
- [50] L. J. Zhou, Z. F. Hou, L. M. Wu, Y. F. Zhang, *J. Phys. Chem. C* **2014**, *118*, 28055.
- [51] F. Banhart, J. Kotakoski, A. V. Krasheninnikov, *ACS Nano* **2011**, *5*, 26.
- [52] J. Ma, D. Alfe, A. Michaelides, E. Wang, *Phys. Rev. B* **2009**, *80*, 1132.
- [53] O. V. Yazyev, S. G. Louie, *Phys. Rev. B* **2010**, *81*.
- [54] V. L. Deringer, A. L. Tchougreeff, R. Dronskowski, *J. Phys. Chem. A* **2011**, *115*, 5461.
- [55] L. J. Zhou, Z. F. Hou, L. M. Wu, *J. Phys. Chem. C* **2012**, *116*, 21780.
- [56] A. D. Becke, K. E. Edgecombe, *J. Chem. Phys.* **1990**, *92*, 5397.
- [57] G. Radhakrishnan, J. D. Cardema, P. M. Adams, H. I. Kim, B. Foran, *J. Electrochem. Soc.* **2012**, *159*, A752.